Computers and Fluids 291 (2025) 106578

Contents lists available at ScienceDirect

Computers and Fluids

journal homepage: www.elsevier.com/locate/compfluid

A data-driven actuator-line methodology for the simulation of high-lift aircraft wake systems

S. Bennie *,[1], P. Nagy [1], M. Fossati [2]

Aerospace Centre, University of Strathclyde, 71 Montrose St., Glasgow G1 1XJ, United Kingdom

ARTICLE INFO

Keywords:
Wake-vortex
Actuator-Line-Method
Aviation-sustainability
Computational-fluid-dynamics

ABSTRACT

The actuator-line method is here integrated with a data-driven approach for the investigation of aircraft-induced trailing vortices as generated by landing and take-off configurations with varying levels of high-lift device deflections. It is shown that through coupling the Actuator-Line-Method to a suitable Reduced-Order-Model built upon spanwise aerodynamic force distributions obtained from high-fidelity CFD solution data. The resulting wake from the geometry can be reproduced in a manner that no longer requires an explicit representation of the aircraft geometry within the simulation environment. The result is a method that allows for increased fidelity in the vortex farfield when studying the relevant wake dynamics and evolution during take-off, climb, approach and landing. The accuracy of the proposed method is assessed via a direct comparison to traditional high-fidelity nearfield derived results where it was observed that the induced downstream velocity profile and resulting location of vortex structures displayed a satisfactory level of agreement. With the creation of such a method, the effects of variations in aircraft high-lift deployment can be included within the simulation of downstream vortex pairs in a manner that respects the computational limitations of current hardware.

1. Introduction

Wake vortices are an unavoidable by-product of the lift generation process. The study of wake vortex phenomena and their interactions are of significant interest to the aviation community in ensuring the continued safe operation of aircraft through assigning reliable and effective mandatory separation distances for aircraft following pattern takeoff/ arrival procedures [1]. The wake-informed mandatory separation matrix has significantly reduced the incidence rates of fatal wake encounters for aircraft operating under Instrument-Flight-Rules. The often conservative weight-based classification matrix has seldom received modification despite significant advancements regarding Computational-Fluid-Dynamics (CFD), parallel computing, and experimental data gathering techniques as applied to the wake-vortex problem [2]. With continual growth in the commercial aviation sector forecast, airports have been left rapidly approaching their maximum theoretical daily capacity limits as set out by such spacing regulations [3,4]. To date, at several of the world's busiest airports, departure/ arrival slots have become the main limiting factor for the continued expansion of daily flight operations [5]. For such airports, the potential benefits a minimal change in separation distance regulations may bring with the creation of new takeoff/ departure slots is considerable [1]. From the perspective of aircraft operators, expenditures attributed to on-ground delays and missed departure/ arrival slots would be substantially reduced. With delayed aircraft expending less fuel in holding patterns on both the ground and in the air, a substantial drop in collective exhaust emissions may also be within reach. At a time where the aviation sector is facing greater scrutiny regarding the transition to greener low-carbon strategies, the environmental benefits of a reduction in aircraft separation standards cannot be understated.

For any alterations to the current aircraft separation standards to be considered acceptable by both aviation authorities and commercial operators, the accompanying theory that such arguments are based must be given in the highest degree of confidence. At the time of writing, case-by-case prediction of wake-vortex dynamics remains highly non-trivial with the variability and stochastic behaviour of wake vortex phenomena making real-time forecasting of downstream encounters a significant challenge. Factors affecting the risk categorisation of an aircraft-wake encounter are numerous with aircraft attitude, altitude, weather and associated atmospheric effects each playing a key role in

* Corresponding author.
E-mail address: Scott.Bennie@strath.ac.uk (S. Bennie).
[1] PhD Student, Department of Mechanical and Aerospace Engineering
[2] Reader, Department of Mechanical and Aerospace Engineering

https://doi.org/10.1016/j.compfluid.2025.106578
Received 29 February 2024; Received in revised form 21 October 2024; Accepted 12 February 2025
Available online 20 February 2025

encounter severity. In cases of sufficient vortex strength, the imposed roll moments induced by a wake-vortex encounter may become greater than the available control authority of the aircraft [6]. Considering aircraft operating at low altitudes where the window for recovery is minimal and fully dependent on aircrew reaction times, the danger posed by wake interactions is greatly increased for aircraft on final approach or take-off. The ability to simulate the wake dynamics of aircraft configured for such operations remains highly limited due to the complex nature of the downstream flow field. Numerous vortex pairs originating from both the wingtip of the main element in addition to the deployed high-lift devices require fine computational grids that become increasingly computationally intensive as the domain reaches dimensions that accurately capture approach/ take-off corridors.

Circumventing the challenge of high-fidelity simulation, several notable fast-prediction solutions making combined use of field deployed sensors and theory have been successfully validated from real-word trials. Examples of which include NASA's Aircraft-VOrtex-Spacing-System (AVOSS) [7] and the Wake-Vortex-Prediction-Monitoring-System (WSVBS) [4,8] deployed at Dallas Ft. Worth and Frankfurt/ Munich airports for field-trials respectively. Both systems performing well highlighted the ability of fast-prediction based methods to systematically reduce separation standards on demand. Industry wide acceptance of such strategies has yet to be fully realised with the majority of regional-authorities opting to remain with classical matrix-based approaches [9]. Key to influencing such a decision is the simplicity and efficacy of standard tabular matrices for the separation distance assignment requiring next to no additional equipment or training for staff to utilise effectively. The favouring of simple matrix-based methods suggests that for any solution to be globally adopted it must remain general enough for broad application to the existing tabular standards rather than on a case by case basis as provided by fast-prediction approaches. To satisfy such a requirement improvements must be made with respect to both our understanding of wake vortex dynamics and our capabilities in simulating realistic scenarios regarding high-lift configured aircraft that accurately reflect the conditions in which wake vortices occur in close proximity to the ground.

With increasing levels of air traffic, it has become clear that a detailed risk assessment must take full account of not just the danger wake vortices pose to aircraft but also to individuals residing in the vicinity of active airfields. The descent of vortex systems over considerable distances, facilitated by the mutual induction of their respective velocity fields poses a credible risk to structures and individuals within the vicinity of active flight corridors. Documented cases of mechanical damage as arising from the exposure of structures to the large swirl velocities and low pressures associated with trailing vortices remains confined to sections of tiled roofing [10,11].

Given the ever increasing capabilities of modern computing, CFD simulation appears poised to play a leading role in the future of wake vortex research. Accurate simulation of downstream aircraft wake environments encompassing all phases from vortex roll-up to farfield decay in a manner that reflects real-world conditions remains a significant barrier to the use of CFD derived results in the wake risk assessment process. A vast separation of length scales coupled with the need to minimise the effects of numerical dissipation, particularly around the vortex core, results in domains that continue to exceed the current capabilities offered by modern computing resources. To circumvent such issues, the specific phenomena of interest dictates the use of a local simulation environment. Studies of the near and mid-field behaviour frequently being performed using high-fidelity RANS [12] or hybrid RANS/ LES methods [13] where the aircraft geometry is directly represented. For the study of vortex farfield dynamics the structures present within the aircraft nearfield cannot be propagated sufficiently within a single domain in a manner that remains computationally feasible. Instead initial conditions are taken from idealised mathematical vortex models through relation to the aircraft properties [1,14–16]. Such model based initialisation approaches remain valid for aircraft in a clean-wing configuration. When considering the complex flow field generated by aircraft in a high-lift configuration the idealised models do not account for the complex contra-rotating inner vortex pairs that are shed by the flap geometries [17]. Contributions of the inner vortex pairs leading to an accelerated decay process frequently alter both the strength and position of the final contra-rotating vortex wake hence suggesting their presence cannot be neglected.

Notable emerging methodologies presented by Zhang et al. and Stephan [18,19] have been developed enabling the full simulation of trailing vortex systems from roll-up through to farfield decay to be conducted within the same computational domain through various means. Zhang et al. [18] in their work promoted the use of a so called "Lift-Drag" method where through the addition of source terms to the governing fluid transport equations the effect of the aircraft geometry could be included within the simulation implicitly [18,20,21]. The "Lift-Drag" model presented by Zhang falling under the branch of Actuator-Surface-Methods (ASMs) applied the local source term values uniformly upon a pre-defined surface embedded within the domain. Values for which were computed based upon an assumed elliptical spanwise load distribution across the aircraft wing, valid for an aircraft in a clean-configuration. For application to the study of wake dynamics in cruise, the "Lift-Drag" method performed satisfactorily with well-matched velocity distributions in the wake region as compared to wind-tunnel data. For aircraft in a high-lift configuration where the spanwise load distributions deviate significantly from elliptical profiles, the analytical derivation of Lift and Drag quantities could no longer be applied.

Stephan in their work proposed the use of an alternative methodology for application to both clean and high-lift configured geometries [19]. By sweeping the solution of a steady-state RANS nearfield simulation throughout the computational domain on a per-timestep basis, a time-accurate vortex wake could be generated allowing for the variations in vortex age to be studied. By directly mapping the velocity and pressure fields from the nearfield RANS data to that of the LES study no details would be lost regarding the downstream flow phenomena enabling the simulation of more complex high-lift trailing vortex pairs. Via the process of sweeping the solution field throughout the LES domain, the vortex would evolve temporally allowing for the inclusion of time dependent behaviour neglected by other methods. Due to the use of a precursor RANS simulation, the computational cost of simulating various high-lift deflection cases would become increasingly expensive due to the large volume of solutions required.

Through the current work a new approach is presented that allows preservation of the key high-lift flow features on display within the wake of the aircraft nearfield and allows propagation to the study of farfield vortex behaviour within a single simulation environment. Using the Actuator-Line-Methodology (ALM), as first proposed by Sørensen and Shen [22] additional source terms are included within the governing fluid transport equations to allow for the effect of the wing geometry to be included implicitly within the simulation environment. Through the removal of the aircraft geometry, grid constraints associated with near surface effects are relaxed allowing for a redistribution of grid points to the downstream phenomena of interest. The result is a significantly simplified simulation domain with an increased grid resolution about the vortex structures of interest allowing the use of higher-fidelity solvers for a similar or reduced computational cost. To allow for the simulation of various high-lift deflection cases, the ALM is coupled with a Reduced-Order-Model (ROM) which once generated from a set of high-fidelity nearfield CFD data with the aircraft geometry present, may be evaluated on demand to initialise the actuator-line method without the need for additional costly precursor simulations. The ALM-ROM approach allowing for the higher-fidelity study of high-lift wakes as they relate to approach and take-off scenarios is thus poised to contribute to a greater understanding of wake vortex phenomena in the near-ground region. The results of which forming the basis of cohesive arguments regarding aircraft separation regulations and the

wider impact of increasing levels of air traffic in terms of sustainability particularly regarding those residing in the vicinity of airports.

The structure of the manuscript is as follows. Within Section 2 an overview of the Actuator-Line-Method is presented and the corresponding coupled ALM-ROM approach for the simulation of high-lift induced wake-vortex systems is introduced. Application of the ALM-ROM approach to the study of an example high-lift geometry and its related wake vortex system is then presented within Section 3. Here the Reduced-Order-Modelling approach is further detailed in combination with methods for validating the accuracy of ROM generated data. Section 4 presents the results of various simulations as they relate to the generation and use of the ALM-ROM approach. Initially the results of conventional simulation of the high-lift geometry are presented with a discussion of the vortex dynamics immediately visible in the aircraft nearfield environment which the ALM-ROM aimed to replicate. Results of the ROM validation tests are subsequently presented and a discussion given regarding the accuracy of the Proper-Orthogonal-Decomposition method for the ALM-ROM application case. The results of various Actuator-Line simulations are then given pertaining to the validation of the ALM-ROM implementation and later an application of the complete method to the study of an aircraft on approach. A final discussion on the applicability of the ALM-ROM method for the simulation of high-lift aircraft wakes is then given with corresponding conclusions within Section 5.

2. Actuator-Line source methodology

The actuator-line method is one of several approaches that seeks to reduce the complexity of simulating the trailing wake environment of lifting bodies through the implicit inclusion of additional source terms within the governing fluid transport equations that represent indirectly the force exhibited from the lifting body on the fluid [22]. By implicitly representing the aircraft geometry, the grid generation process becomes significantly simplified allowing for the use of structured meshing strategies combined with greater levels of refinement surrounding the wake vortex phenomena as compared to standard CFD nearfield simulations. Sufficiently refined grids are of particular importance for the study of high-lift wake vortex phenomena where it becomes necessary to maintain a high level of resolution over downstream distances exceeding eight wingspans to accurately capture the long-wave instability mechanism that initiates vortex decay patterns [23].

The ALM within recent years has experienced moderate adoption within the field of aeronautics, particularly for the study of rotorcraft induced vortical structures [22,24] and higher-accuracy simulation of distributed-propeller aircraft designs [25]. Actuator based methods have only recently been extended to the field of fixed-wing study in using source terms to emulate the effects of lifting-surfaces for the purposes of studying the downstream wake environment [20,21,26].

With reference to the governing equations of a compressible fluid given by Eq. (1) [27]. Following exposure of a lifting surface to an external flow field, forces are generated both perpendicular and normal to the direction of fluid motion. From Newton's third law, a fluid element experiences an equal but opposite force applied from the body. In the context of an Eulerian reference frame these forces can be considered as source terms acting upon the nodes that comprise the volumetric grid, given by Eqs. (2)–(4), below.

$$\mathcal{R}(U) = \frac{\partial U}{\partial t} + \nabla \cdot \bar{F}^c(U) - \nabla \cdot \bar{F}^v(U, \nabla U) - S = 0 \tag{1}$$

$$U = \begin{Bmatrix} \rho \\ \rho\bar{v} \\ \rho E \end{Bmatrix} \quad \bar{F}^c = \begin{Bmatrix} \rho\bar{v} \\ \rho\bar{v} \otimes \bar{v} + \bar{\bar{I}}p \\ \rho E\bar{v} + p\bar{v} \end{Bmatrix} \quad \bar{F}^v = \begin{Bmatrix} \cdot \\ \bar{\bar{\tau}} \\ \bar{\bar{\tau}} \cdot \bar{v} + \kappa\nabla T \end{Bmatrix}$$

$$\mathcal{R}_{\mathrm{ALM}}\left(\frac{\delta\rho}{\delta \mathrm{t}}\right) = 0 \tag{2}$$

$$\mathcal{R}_{\mathrm{ALM}}\left(\frac{\delta\bar{v}}{\delta \mathrm{t}}\right) = -\bar{F} \tag{3}$$

$$\mathcal{R}_{\mathrm{ALM}}\left(\frac{\delta \mathrm{E}}{\delta \mathrm{t}}\right) = -\bar{F}.\bar{v} \tag{4}$$

where $\boldsymbol{\rho}$ is the freestream density, $\bar{\mathbf{v}}$ is the freestream velocity, $\mathbf{E}$ is the energy per unit mass, $\bar{\mathbf{F}}$ is the applied force of the actuator line node, $\bar{\bar{\boldsymbol{\tau}}}$ is the viscous stress tensor, $\boldsymbol{\kappa}$ is the thermal conductivity and $\mathbf{T}$ is the temperature.

The source terms of the ALM require as input the components of the aerodynamic force, $\bar{F}$ as prescribed at discrete points along the span of the wing geometry. For simple wing designs these values may be obtained analytically through the evaluation of two-dimensional airfoil theory. Regarding more complex multi-element designs such as the aircraft considered presently, the authors propose a numerical approach whereby high-fidelity nearfield CFD of the target geometry is initially performed. Through the piecewise integration of the surface pressure solution along the span of the geometry, given via Eq. (5), the spanwise distribution of the vertical and horizontal components of the aerodynamic force may be obtained.

$$\bar{F} = \oint pn \, \mathrm{dA} \tag{5}$$

where $\bar{\mathbf{F}}$ is the force generated by the integral section, $\mathbf{p}$ is the pressure, $\mathbf{n}$ is the normal unit vector, and $\mathbf{A}$ is the area of the integral section.

Throughout the current work, the surface pressure solution is obtained from simulations performed within a body-fixed reference frame, hence for the integration process of Eq. (5) the computed force corresponds to the components of the aerodynamic force as applied in the body-fixed frame. For the spanwise force distributions presented within the current work the non-dimensionalised spanwise position is used, calculated using the semi-span of the example high-lift geometry.

By performing the integration process over discrete sections of the aircraft span, the three-dimensional wing is reduced to a series of discrete points that are taken to lie upon the local aerodynamic centre of the section. The collection of these points and their computed components of the aerodynamic force form the actuator-line as illustrated by Fig. 1, denoted in red is the actuator-line with glyph arrows displaying the computed components of the aerodynamic force which would be applied via Eqs. (2)–(4). For the purposes of illustration, the actuator-line was generated using 20 integral sections. To ensure the spanwise data accurately captured the local force distributions, 150 equidistant integral sections were used in the present work.

For the study of geometries that feature varying levels of high-lift deployments, the need to perform nearfield simulations in order to generate spanwise force data as required to initialise the ALM source terms becomes prohibitively expensive. To solve this, the ALM is here coupled with a Reduced-Order-Model (ROM) based upon Proper-Orthogonal-Decomposition (POD). Once created, the ROM allows for the on-demand generation of spanwise force data for flap deflection angles that have not been simulated explicitly. The general ALM-ROM process is detailed within Fig. 2. Following the description of the geometry and its associated high-lift deflection angles, nearfield simulations are performed for various points across the deployment envelope. From the solutions of simulating the high-lift geometry explicitly, the spanwise distribution of aerodynamic force components may be derived via Eq. (5). Using the spanwise data as input, the ROM is thus generated which upon evaluation provides spanwise distribution data for the desired high-lift deflection case without the need for further costly nearfield simulations of the aircraft. Following the validation of the ROM predictions, the spanwise force given by the model may be used to initialise the source terms of the actuator-line allowing for propagation of the wake-vortex structures in a simulation environment where the aircraft geometry is no longer represented explicitly.

Within the current work, the ALM-ROM process is presented as it was applied to an example high-lift geometry exhibiting various degrees of flap deployments. Initially four flap deflection angles are considered and the corresponding nearfield simulations of the aircraft

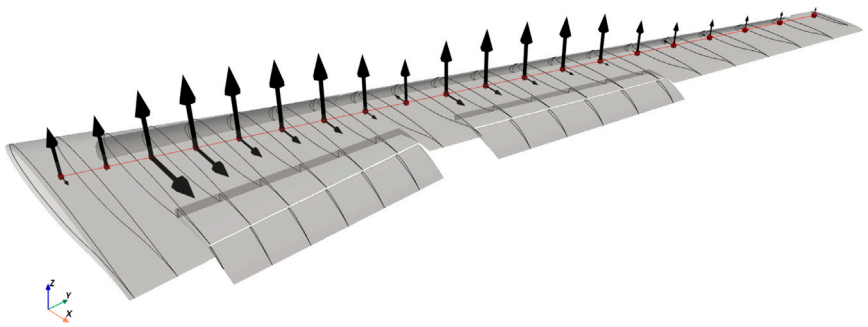

Fig. 1. Decomposition of high-lift geometry to actuator-line representation.

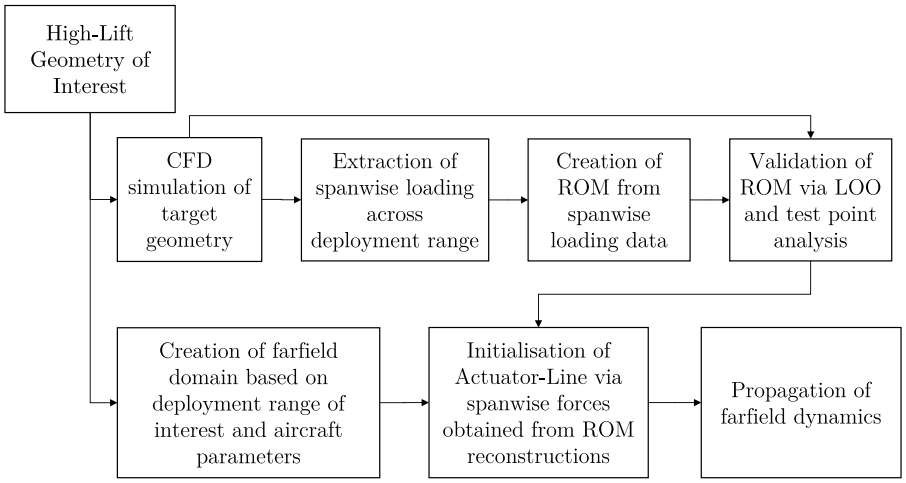

Fig. 2. Coupled ALM-ROM process chart.

are performed for the purposes of obtaining the spanwise data. From this data the ROM is generated and its accuracy assessed via both a Leave-One-Out analysis and a direct comparison to data obtained from further simulations of the high-lift geometry. Further information regarding the formulation of the ROM and the validation process are detailed within Section 3.5. The overall ALM-ROM approach is then validated by comparing the wake vortex structures as observed within the results of simulations performed via conventional explicit representations of the aircraft geometry to its equivalent actuator-line counterpart. A final application case of the ALM-ROM approach is later presented where the actuator-line is swept throughout the computational domain on a per timestep basis representative of an aircraft following a typical approach trajectory.

3. Numerical setup

3.1. High-lift geometry of study

The subject of study within the current application of the ALM-ROM approach was the modified Energy-Efficient-Transport-Aspect-Ratio 12 (EETAR12) [28]. Initially scaled to a wingspan representative of a medium-haul aircraft design, the EETAR12 was chosen due to its availability within the OpenVSP geometry package coupled with the published high-lift deployment configurations given by Olsen [29]. The design incorporated double span slotted vane/ flap sections together with leading edge slats. Table 1 lists the main geometric parameters of the modified design. For the purpose of obtaining the spanwise force distributions required to generate the ROM, simulations of the EETAR12 were performed upon the semi-span of the aircraft with only the wing geometry present.

Table 1
Geometric parameters of the modified EETAR12 Aircraft.

Semi-Span	18.0 m
Sweep	26.0 deg
Dihedral	4.5 deg
Root chord	6.2 m
Tip chord	1.5 m
Mean aerodynamic chord	3.5 m

Prior to simulation several geometric simplifications were made to the original design each contributing to improving the overall surface topology and thus guaranteeing the quality of the final surface grid. Modifications comprised of the substitution of slotted vane/ flap sections with equivalent continuous geometries, blunting of aerofoil trailing edges, and sharpening of the flap recesses within the main wing.

For the generation of spanwise distributions that would form the input dataset for the Reduced-Order-Model, four discrete high-lift deflection angles were considered, termed configurations presently. Numbered one to four, the configurations corresponded to EETAR12 geometries exhibiting the minimum up to the maximum possible flap deflection angles respectively. For each configuration, the leading edge slats remained in a fixed deployed state. For validation tests regarding the ROM and the ALM-ROM coupled approach, simulations for three further intermediate flap deployment states that lay between the discrete configurations used in generating the ROM were performed. Tables 2 and 3, include the high-lift deflection angles, θ, for both the four initial simulations used in generating the ROM and the three intermediate test-points used in validation tests respectively.

Table 2
EETAR12 high-lift deflection angles for discrete configurations within deployment envelope.

Geometric Entity	Flap setting	θ (deg)
Inner flap	1	8.9
	2	17.7
	3	26.6
	4	35.5
Outer flap	1	9.6
	2	19.1
	3	28.7
	4	38.2
Inboard slat	Fixed	−34.7
Outboard slat	Fixed	−34.4

Table 3
EETAR12 high-lift deflection angles for intermediate configuration test points.

Geometric entity	Test point	θ (deg)
Inner flap	1	10.6
	2	24.8
	3	31.0
Outer flap	1	11.5
	2	26.8
	3	33.4
Inboard slat	Fixed	−34.7
Outboard slat	Fixed	−34.4

Table 4
Properties of the prism layer mesh.

First layer thickness	1e−6
Geometric progression ratio	1.268
Number of layers	42

3.2. Grid generation

Grid generation was performed using the open-source GMSH software [30] for the explicit simulation of the EETAR12 geometry and for the actuator-line simulations presented within Section 4.

3.2.1. EETAR12 nearfield

For the high-fidelity simulation of the EETAR12 nearfield. Across the main wing and high-lift surfaces, a structured meshing approach was employed where possible, ensuring high-quality prism-layers could later be inserted. Due to instantaneous changes in chord length about the flap regions, small transition segments were unavoidable within the geometry as also noted by Olsen [29]. Problem regions were identified and repaired using manual meshing tools to approximate a structured grid in areas for which a complete structured approach was not possible. A smooth transition of elements from the aircraft surface to the surrounding volume was achieved through enforcement of various sizing constraints. Additional local refinement was performed around the high-lift devices with emphasis placed upon ensuring the channel regions created between the flap and main wing were well captured by the grid. Following the generation of the inviscid grid, prism layers were inserted via an advancing normal procedure [31]. Initial values for the prism insertion process were taken from the analytical solution for a turbulent flat plate at equivalent freestream conditions. The prism layer growth rate and first element thickness were altered in an iterative manner until a final grid setup was reached that ensured $y^+ \leq 1$ across the surface. The final properties of the prism layer are summarised within Table 4.

Four rounds of solution based volumetric mesh adaptation was performed to improve the quality of the EETAR12 grids. Due to the stochastic nature of the mesh adaptation process, grid convergence was assessed via considering the derived spanwise distributions obtained from intermediate adaptation stages. Fig. 3 provides a plot of the derived spanwise distribution for flap configuration three for each of the grid adaptation stages. The final EETAR12 grids consisted of $\sim 17 \times 10^6$ nodes, subject to the particular high-lift configuration of interest.

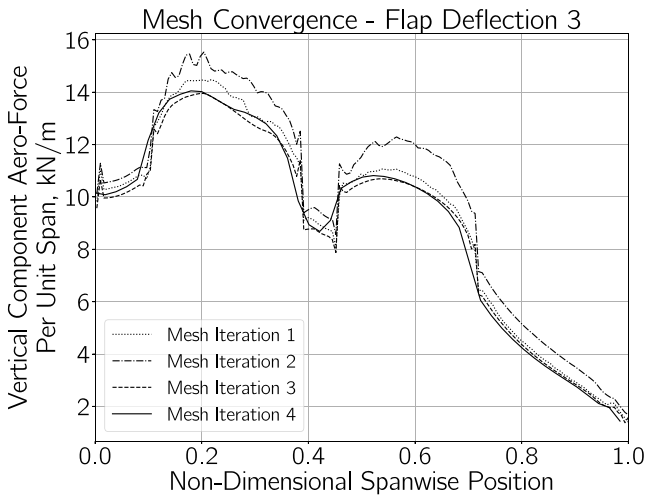

Fig. 3. Convergence of vertical aerodynamic force component across mesh adaptation stages, Flap configuration 3.

Farfield boundary conditions were imposed on all circumferential outer surfaces of the volume with a symmetry condition enforced at the face representing the wing-fuselage junction. Across the surfaces exposed to the flow, no-slip conditions were applied. The farfield was positioned at a distance of fifteen chord lengths, minimising the influence of pressure reflections upon the final solution.

3.2.2. ALM-ROM simulations

Regarding results obtained with the ALM-ROM approach two grids were generated, a body-fixed case for steady-state ALM validation simulations which represented the semi-span of the EETAR12 geometry through the actuator-line and a ground-fixed grid for demonstration of the capabilities of the ALM-ROM method for the study of an aircraft on approach where a full-span of the EETAR12 via the actuator-line was simulated.

In using the ALM-ROM approach, the grid generation process was significantly simplified with the removal of the EETAR12 geometry from the domain. To ensure the ALM source terms were applied consistently, the actuator-line was embedded within the computational domain directly. A curvilinear structured approach was then adopted focused upon the location of the actuator-line. For both ALM-ROM simulations, in the spanwise direction where the actuator-line nodes would be distributed a uniform spacing was applied consisting of 150 discrete points, consistent with the integral sections used in generating the spanwise loading input data. Geometric biases were used to progressively cluster cells within the vicinity of the actuator-line minimising any possible numerical dissipation induced by the grid.

Best practices for the numerical simulation of wake vortices suggests a minimum of three cells be present within the vortex core region to minimise the effect of grid dissipation [21]. For high-lift wakes, the downstream environment would be complicated by the addition of several inner vortex pairs. To remain consistent, the assumed tip vortex dimensions were used to determine the appropriate grid spacing in the spanwise dimension. Estimation of tip vortex core radii is the subject of uncertainty with experimental data suggesting a value of ≈1% of the aircraft span [32]. Numerical studies of farfield vortex behaviour relax this assumption to 2–8% to maintain grids that remain computationally reasonable. For the ALM cases presented within Section 4, a grid resolution of $\Delta_{\mathrm{ALM}} = 0.066$ m was used which assuming a vortex core

radius of 1% span resulted in a grid which possessed ≈5 nodes within the core regions.

The dimensions for the steady state ALM validation simulations spanned a domain of $l_x = 51.5$ m, $l_y = 76$ m, $l_z = 40$ m with $n_x = 309, n_y = 360, n_z = 200$ comprising of $\sim 22 \times 10^6$ grid points. Farfield boundary conditions were imposed on all faces with the exception of a symmetry plane on the face representing the wing-fuselage junction.

For the unsteady ALM ground study, the domain dimensions comprised of $l_x = 216$ m, $l_y = 72$ m, $l_z = 50$ m with $n_x = 615$, $n_y = 189$, $n_z = 181$, totalling $\sim 28.9 \times 10^6$ grid points. To ensure the Kelvin–Helmholtz theorem remained satisfied periodic boundaries were used on all faces with the exception of the top and bottom surfaces. No-slip conditions were enforced at the face representing the ground plane and an accompanying slip condition was applied at the upper surface of the domain.

3.3. Flow solver

All simulations were conducted using the open-source Stanford University Unstructured (SU2) CFD solver in varying configurations [27]. The choice of SU2 was motivated by its modular structure which allowed for straightforward implementation of the ALM source terms within each of the individual solver class structures.

EETAR12 nearfield simulations were performed solving the steady-state Reynolds-Averaged-Navier–Stokes (RANS) equations together with the Spalart–Almaras (SA) turbulence model for the semi-span wing geometry. The SA turbulence model was chosen for its inherently lower-cost, being a one-equation model, in addition to its well-documented performance for aircraft applications [33]. Convective fluxes were obtained using the Jameson-Schmit-Turkel (JST) scheme. Use of the JST scheme compared to less dissipative alternatives was driven by its relative robustness in dealing with complex geometries, particularly regarding the flap alcove and leading edge slat regions. Freestream conditions for the nearfield EETAR12 simulations are provided within Table 5. From the conditions listed and using the MAC of the EETAR12 geometry, the Reynolds and Mach number for the flow was 16.2×10^6 and 0.2 respectively typical for a medium-haul aircraft operating at low altitudes. ALM validation cases where the domain remained body fixed were performed via the steady-state RANS solver in an identical configuration as to the EETAR12 nearfield.

For the application of the ALM-ROM to the study of an aircraft on approach in a ground fixed environment, the unsteady hybrid RANS-LES solver was employed using a second order dual time stepping approach with a fixed timestep of 5×10^{-3} s. Subgrid terms for the hybrid RANS-LES simulation were obtained using a Smagorinsky SGS model. Freestream conditions were initialised to remain identical to the original simulations of the EETAR12 geometry ensuring a consistent solver environment that allowed for direct comparisons to be made between the EETAR12 nearfield result and those generated by the ALM-ROM approach. Simulation properties for each case are summarised within Table 5.

3.4. Extraction of EETAR12 spanwise loading

From the result of the four initial EETAR12 nearfield simulations, the spanwise load distribution was computed through the integration of the pressure solution as given by Eq. (5). For this work, only the pressure contributions to the overall aerodynamic force was considered. Assumed valid due to the minor contributions of the skin-friction to the overall wing loading.

Table 5
Solver properties for nearfield and ALM-ROM simulations.

Simulation case	EETAR12 Nearfield	ALM-ROM Steady	ALM-ROM Unsteady
High-lift configuration	Fixed	Variable	4
Solver	RANS	RANS	LES/ RANS
Subgrid scale	N/A	N/A	Smagorinsky
Timestep (s)	N/A	N/A	5e−3
Mach	0.2	0.2	0.2 (Represented by translating ALM)
AoA (Deg)	2.4	2.4	2.4
Density (kg/m^3)	1.20282	1.20282	1.20282
Temperature (K)	288.15	288.15	288.15

3.5. Reduced-order-modelling

The ROM coupled to the ALM was the data-driven non-intrusive approach based upon Proper Orthogonal Decomposition, adopting specifically the *method of snapshots* algorithm for generation of the low-order model [34]. In this case the snapshots would be formed of the spanwise load distribution data obtained from the discrete simulation of the high-lift geometry. Predictions of the spanwise loading for untested flap deflection cases were obtained using an approach similar to that presented by Bui-Tanh et al. [35], therefore coupling the ROM with Radial Basis Function (RBF) interpolation.

In general through the POD approach, the approximate high-dimensional solution manifold is represented in a low-order linear space by extraction of the *optimal* basis functions (or POD modes) from the training data or *snapshot set*. The modes are considered optimal because the error between the solution and the reduced representation is minimised under the Euclidean norm. Formally, the optimal basis functions are found by solving the maximisation problem [36]:

$$\max_{\psi} \frac{\langle |(\mathbf{U}, \boldsymbol{\psi})^2| \rangle}{(\boldsymbol{\psi}, \boldsymbol{\psi})} = \frac{\langle |(\mathbf{U}, \boldsymbol{\phi})^2| \rangle}{(\boldsymbol{\phi}, \boldsymbol{\phi})} \tag{6}$$

where $\mathbf{U}$ is the snapshot set: $\{\mathbf{u}_1, \mathbf{u}_2, \ldots, \mathbf{u}_{N_s}\}$ for N_s CFD solutions, and $\boldsymbol{\phi}$ are the optimal basis functions while $\boldsymbol{\phi}$ are the prospective basis functions. The operators $(\cdot, \cdot)$ and $\langle \cdot \rangle$ denote the inner product and averaging across the parameter space respectively.

For the algorithm adopted in the current work it can be shown that the modes are a linear combination of the snapshot set:

$$\boldsymbol{\phi}_i = \sum_{j=1}^{N_s} b_j^i \mathbf{u_j} \tag{7}$$

for $i = 1, 2, \ldots, N_s$. $\mathbf{u_j}$ is the quantity of interest for snapshot j, and b_j^i is the associated POD coefficient. Then, the coefficients b_j^i satisfy the eigenvalue problem:

$$\mathbf{R}\mathbf{b}_i = \lambda_i \mathbf{b}_i \tag{8}$$

where $\mathbf{R} = \mathbf{U}^T\mathbf{U}$, i.e. the cross-correlation matrix of the snapshots. The eigenvalues λ_i correspond to the energy of each mode which allows for them to be ranked and truncated based on their energy content and a threshold value [35]. The normalised POD modes are obtained after solving the eigenvalue decomposition and are expressed as:

$$\boldsymbol{\phi}_i = \frac{1}{\sqrt{\lambda_i}} \mathbf{U}\mathbf{b}_i \tag{9}$$

The approximate solution $\hat{\mathbf{u}}$ at an arbitrary $\mathbf{x}$ location in the parameter space is expressed as a linear combination of the modes ϕ_i and coefficients, a_i. The latter are obtained via RBF interpolation. Thus, a reconstructed solution is computed as:

$$\mathbf{u}(\mathbf{x}) \approx \hat{\mathbf{u}} = \sum_{i=1}^{N_m} a_i \boldsymbol{\phi}_i(\mathbf{x}) \tag{10}$$

Evaluation of the ROM was performed via two approaches to estimate the error within the reconstructed spanwise distributions, comprising a Leave-One-Out (LOO) analysis and direct comparison to additional simulated high-lift deflection configurations that were not included within the generation of the ROM.

A Leave-One-Out analysis also known as cross-validation [37], refers to the process of validating the ROM using only the training data from which it was first generated. By systematically excluding each training data point from the generation stage of the model a set of depleted ROMs are obtained. Evaluating each depleted ROM to recreate their corresponding excluded data point allows a direct comparison to be made between the ROM generated results and the true spanwise load distribution for the excluded data point. The LOO analysis thus providing an indication of the error present in the ROM predictions. This process is advantageous as it allows for only the original training data to be used for validation compared to requiring additional expensive to compute test-points. The error however remains an estimation due to the use of each depleted ROM as compared to the final model as generated by including all training data points. To ensure the parameter space remains bounded, any training data which falls upon the perimeter of the space must remain. For the four configuration parameter space present in the current work only configuration two and configuration three may be used for a LOO analysis.

To further estimate the error of the complete ROM as used in the coupled ALM-ROM approach, a comparison to three additional flap deflection angle cases was performed, the deflection angles of the test points being included within Table 2. The combined result of the LOO analysis and test-point comparisons allow for the spanwise aerodynamic force component predictions made by the ROM to be included with confidence within simulations incorporating the ALM-ROM approach.

3.6. Initialisation of Actuator-Line simulations

Following the creation of the ROM from the spanwise distributions of the four high-fidelity EETAR12 simulations, the coupled ALM-ROM approach could be used to initialise simulations employing the actuator-line for additional flap deflection configurations for which no spanwise loading data was available.

The ROM was called on demand to provide the spanwise aerodynamic force component distributions for additional flap deflection configurations for the initialisation of the actuator-line source terms. To avoid the occurrence of numerical singularities that may arise when applying the derived force terms directly upon a single point, a convolution step was required. The convolution step transforming the discrete nodes of the Actuator-Line to a point cloud representation. The convolution process followed the method of Mikkelsen [22,38] in adoption a series of two-dimensional Gaussian distributions compared to a completely three-dimensional process as observed within the work of Sørensen. By selecting the two-dimensional process, the distribution of nodal forces would remain strictly limited to the geometrical span of the wing.

Convolution of the spanwise force distributions along the actuator-line was completed via the scaling procedure described by Eq. (11) below. The choice of smearing factor, ϵ, and by association the degree of force re-distribution among surrounding nodes is the subject of discussion within ALM modelling approaches. Values of ϵ may either remain fixed or feature a dynamic variation where the ratio of ϵ to the local airfoil chord length remains constant [39,40]. For the current ALM implementation the former scaling via the local chord was performed, described by Eq. (12). All actuator-line simulations performed presently maintained a value of 0.2c for the calculation of ϵ.

$$\bar{F}_{Smoothed} = \frac{1}{\epsilon^2 \pi} \exp\left(\frac{-r^2}{\epsilon^2}\right) \cdot \bar{F}_{Node} \tag{11}$$

$$\frac{\epsilon}{c} = \text{Constant} \tag{12}$$

where $\bar{\mathbf{F}}_{\mathbf{Smoothed}}$ is the contribution of the original nodal force to the grid point, ϵ is the smearing parameter, $\mathbf{r}$ is the two-dimensional distance of the node from the original point on the actuator-line, $\bar{\mathbf{F}}_{\mathbf{Node}}$ is the original nodal force as generated by the spanwise loading and $\mathbf{c}$ is the local chord length of the section. To remain consistent with the total integrated force quantities of the aircraft wing, the distributed force values were scaled by the original value of the nodal ALM force thus preserving the total vertical and horizontal components of the aerodynamic force.

Initialisation of the steady-state ALM validation simulations where the actuator-line remained fixed in space was performed by evaluating the ROM for the generation of spanwise data at the flap deflection angles of each test point case. As the Actuator-Line remained fixed in space, the applied force as dictated by the convolution step remained unchanged.

For the unsteady ALM-ROM simulation the actuator-line would be simulated traversing a ground-fixed reference frame following an approach trajectory. By computing the position of the aircraft based upon the freestream velocity of the EETAR12 simulations, the actuator-line source terms were varied dynamically to match the local position of the actuator-line at each timestep. To maintain a periodic boundary condition the domain was extended and a mirror image reflection of the actuator line performed. Simulation of the complete span of the EETAR12 aircraft was accomplished via reflection of the relevant spanwise load distributions made by the ROM.

4. Results and discussion

Fig. 4 presents the results of simulating explicitly the EETAR12 aircraft geometry at flap deflection configuration one and four respectively. Corresponding to the bounds of the flap deployment envelope, the figure illustrates the significantly altered wake dynamics that arose with greater deflections of the flap sections, an effect that the ALM-ROM approach aimed to replicate. Provided are contour plots of the vorticity magnitude at set locations downstream of the EETAR12 geometry allowing for the identification of wake vortex structures and their evolution in the wake of the aircraft. A total of five wake vortices were observed within the downstream region of the EETAR12 as illustrated by the concentrated regions of vorticity within Fig. 4. Vortex structures were generated corresponding to the tip of the main wing in addition to the root and tip vortices for both of the flap sections consistent with previous studies [17]. With greater flap deflection values, the strength of the inner vortex pairs was observed to proportionally increase leading to stronger vorticity and larger core radii when comparing the results for the four flap deflection angle simulations at identical downstream locations. The results illustrate the capabilities of conventional RANS simulation for the study of the immediate aircraft nearfield with key features such as the shed vorticity sheet being well resolved. Considering the computational grid used for each of the four EETAR12 simulations, the challenge of propagating the wake vortex systems sufficiently downstream becomes apparent. Of the $\sim 17 \times 10^6$ points comprising the domain, 70% were required for resolution of the boundary layer region alone leaving a significant shortfall in the wake domain at large downstream distances from the aircraft. Despite volumetric mesh adaptation refining in the direct proximity of the vortex structures, the downstream visualisation of the wake structures was impacted significantly by the coarsening of the grid in order to respect the computational limitations of the HPC on which the simulation was performed.

To obtain the spanwise distributions that formed the input data for the generation of the ROM, the surface solutions of the explicit simulation of the EETAR12 aircraft for the four flap deployment configurations given within Table 2 were processed according to Eq. (5) using a total of 150 integration sections. Plotted within Fig. 5 are the spanwise force distributions as obtained from the four simulations of the EETAR12 geometry with the spanwise distance being non-dimensionalised by the semi-span of the EETAR12 aircraft.

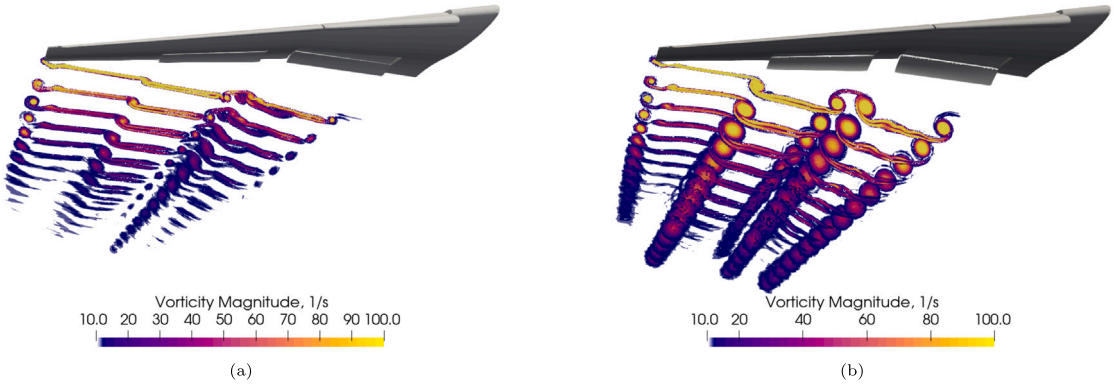

Fig. 4. Contours of trailed vorticity magnitude downstream of EETAR12 flap configuration One (Left), Four (Right).

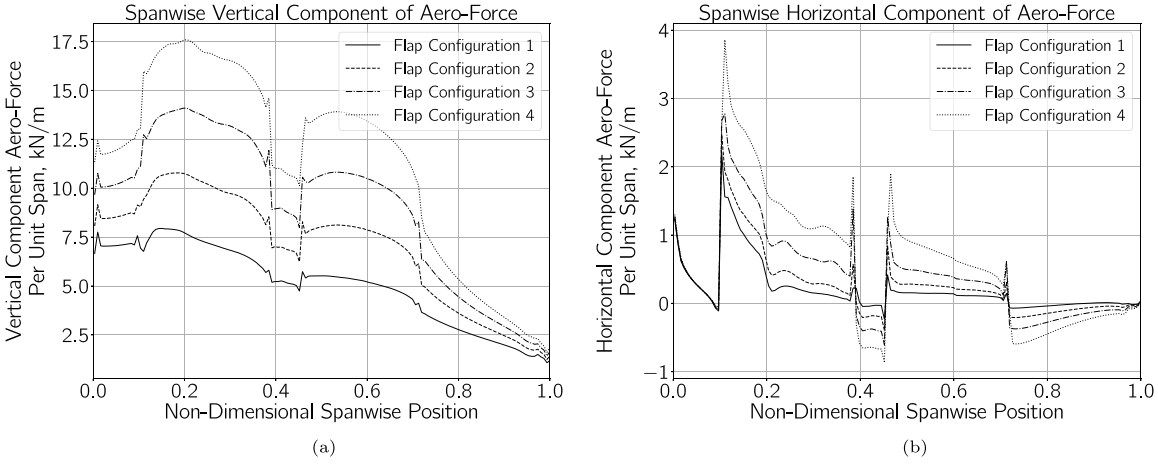

Fig. 5. Spanwise load distributions across High-Lift deflection cases.

Across each of the four flap configurations, deviations from elliptical loading could be observed corresponding to the high-lift devices, where with the extension of the local chord and increased sectional area significantly more lift/ drag was produced. The degree of deviation observed in the spanwise plots was directly correlated with the flap deflection angle. Configuration one possessing the lowest flap deflection angle exhibited a minor divergence from an elliptical profile in the spanwise plots whereas configuration four with the greatest flap deflection angle showed large discontinuities surrounding the flap regions. The magnitude of these deviations contributing to the increased strength and radii of the vortical structures observable within Fig. 4.

Regarding the present case, the EETAR12 flap configuration cases were simulated at a single angle-of-attack assumed typical for an aircraft conducting approach operations. With longer timescales and during varying atmospheric conditions parameters such as the flight speed and angle-of-attack would be expected to fluctuate. For such cases, these parameters could be included within the formulation of the ROM increasing the robustness of the coupled ALM-ROM approach.

4.1. Validation of ROM spanwise distribution data

Following generation of the Reduced-Order-Model from spanwise data extracted from the four nearfield EETAR12 simulations, validation of the ROM generated spanwise force distributions was performed to ensure accurate initialisation of the ALM source terms. Validation was performed via a combination of a LOO analysis in addition to direct comparisons to spanwise distribution data obtained from a further three explicit simulations of the EETAR12 geometry at flap deployment angles that were not previously included within the formulation of the ROM. The flap deflection angles of the three test point cases are included within Table 3.

The LOO analysis was performed through the generation of two depleted Reduced-Order-Models by excluding the spanwise data for flap configuration two and three from the input dataset respectively. Evaluating each depleted ROM for the spanwise force distributions corresponding to their excluded data point, the plot within Fig. 6 was obtained with the values of the computed error presented via Table 6. Denoted in solid lines are the true spanwise distributions as obtained from the explicit simulation of EETAR12 with the corresponding dashed lines representing spanwise data as generated by the depleted ROMs. Within Table 6 the average and maximum errors in the depleted ROM predictions for both the horizontal and vertical components of the aerodynamic force are given combined with the range of the original data.

Comparing the plots of Fig. 6, the model appeared highly-effective at replicating the spanwise loading distributions for both the horizontal and vertical force components. Across both of the spanwise distributions deviations appeared visible with the magnitude of which being minimal for the majority of the plots. Considering the computed error values further illustrates the accuracy of the ROM with the mean error values being very low when compared to the average of the data. The maximum error within the distributions however was moderately greater in comparison, occurring at the discontinuities in the spanwise plots caused by the flap sections. Comparing relative values the prediction of the horizontal aerodynamic force component possessed the largest error for both of the two ROM predictions considered. This was a consequence of the overall magnitude of the horizontal force components being significantly smaller in comparison to the vertical

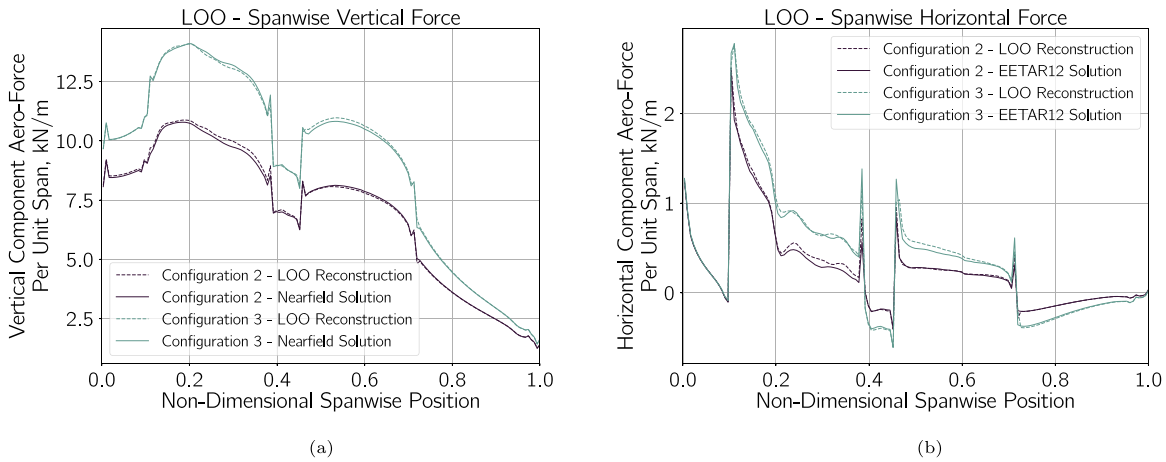

Fig. 6. Spanwise vertical component of aerodynamic force (Left), Horizontal aerodynamic force component (Right) for data generated by depleted reduced-order-models and results of explicit EETAR12 geometry simulation.

Table 6
Computed error values between spanwise load distributions obtained from depleted ROMs and corresponding excluded training data.

	$Error_{mean}$ (kN/m)	$Error_{max}$ (kN/m)	$Data_{max}$ (kN/m)	$Data_{min}$ (kN/m)	$Data_{mean}$ (kN/m)
Flap Configuration 2 - F_z	−0.0420	0.402	10.783	1.250	7.003
Flap Configuration 2 - F_x	−0.017	0.254	2.480	−0.4	0.260
Flap Configuration 3 - F_z	−0.018	0.414	14.096	1.430	9.075
Flap Configuration 3 - F_x	−0.011	0.252	2.775	−0.608	0.386

Table 7
Computed error values between spanwise load distribution obtained from ROM and EETAR12 test point simulation data.

	$Error_{mean}$ (kN/m)	$Error_{max}$ (kN/m)	$Data_{max}$ (kN/m)	$Data_{min}$ (kN/m)	$Data_{mean}$ (kN/m)
Test Point 1 - F_z	0.030	0.084	8.494	1.118	5.500
Test Point 1 - F_x	−0.006	0.030	2.260	−0.265	0.208
Test Point 2 - F_z	0.044	0.403	13.303	1.374	8.692
Test Point 2 - F_x	−0.001	0.156	2.589	−0.567	0.347
Test Point 3 - F_z	0.100	0.462	15.844	1.513	10.267
Test Point 3 - F_x	−0.011	0.176	3.223	−0.746	0.467

force predictions. As the main contributor to the formation of the vortical structures in the wake was the vertical component of the aerodynamic force, the effect of the error within the horizontal force components was minimal.

Validation of the full ROM formulated from the complete set of spanwise distribution data was performed through comparison to data derived from the explicit simulation of EETAR12 geometry at additional flap deflection angles within the deployment envelope. The predictions of spanwise force data as obtained from the ROM and the EETAR12 simulations are plotted within Fig. 7 with the computed errors given by Table 7. Consistent with the results of the LOO analysis, the full ROM was able to predict to high level of accuracy the spanwise distribution of forces for the three test point flap deflection angles. The largest error continued to occur about the discontinuities within the plots caused by the high-lift sections. Notably the mean error for test point three was the largest illustrated also within the plots of Fig. 7. This was considered a result of the discontinuities caused by the flap sections becoming larger with greater deflection of the flap geometries. The ROM therefore performed best for intermediate flap deflection angles lower than that of flap configuration three suggesting a greater sampling of nearfield solution derived input data may be required within this region for future applications of the ALM-ROM to the EETAR12 case. With satisfactory results from both analysis, the ROM was considered validated for use in subsequent simulations of the high-lift geometry via the coupled ALM-ROM approach.

4.2. ALM-ROM validation

Following validation of the ROM generated spanwise load distributions, the implementation of the coupled ALM-ROM approach within the SU2 flow solver was assessed through comparison of the induced wake vortex structures generated by the explicit simulations of the EETAR12 geometry to their ALM-ROM counterpart. Comparisons were performed by comparing the results of the three test case flap deflection cases where the actuator-line would be initialised based upon the spanwise load data provided by the ROM. Across each of the three cases an identical flow solver setup was used to ensure accurate comparisons could be made. The actuator-line in this case representing the semi-span of the EETAR12 aircraft geometry. Below Figs. 8 and 9 plot side-by-side the results obtained from the simulation of the EETAR12 geometry (right) and the ALM-ROM equivalent (left) for test point configuration one and three respectively. Note that in the case of the ALM-ROM results, the results have been reflected to allow the two sets of data be plotted side by side for comparison purposes. Plotted are isosurface contours of the Q-Criterion which allowed for the identification of vortex structures as closed cylindrical surfaces. The figure represents the EETAR12 geometry and actuator-line representation upstream with the trailing vortices present at the forefront of the plot. Included also is a contour plot of the vorticity magnitude for a two-dimensional slice of the domain taken 10 m downstream in both cases. This slice representation shows the planar data for which a quantitive analysis of the wake structures is later performed. Visible within the results of the EETAR12 simulations are the five distinct wake vortex structures and associated wake vortex sheet shed from the main element and flap sections independently as discussed for Fig. 4. Considering the results obtained from the ALM-ROM approach on the left of the plots, the key wake vortex structures appeared well matched in the downstream region both in terms of position and overall core radius. Notably absent

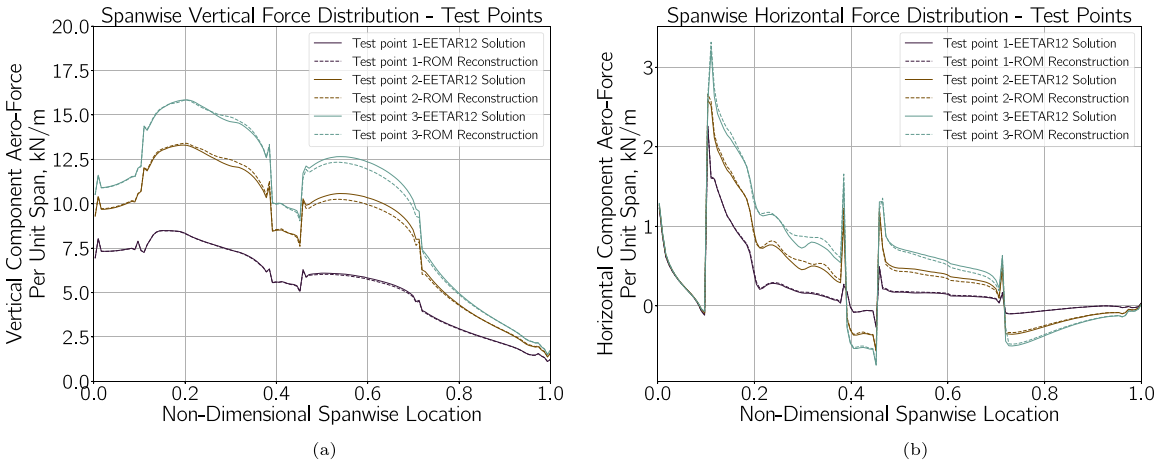

Fig. 7. Spanwise vertical component of aerodynamic force (Left), Horizontal aerodynamic force component (Right) for data generated by complete reduced-order-model and results of explicit EETAR12 geometry simulation.

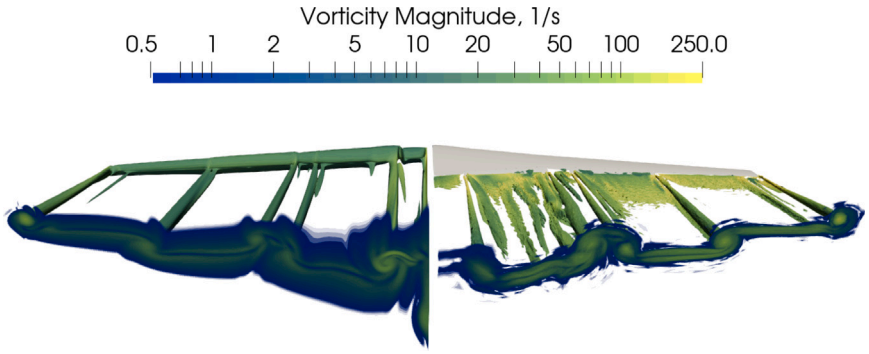

Fig. 8. Test Point 1 - Isosurfaces of Q-Criterion = 50 for ALM-ROM (Left), EETAR12 Explicit Simulation (Right).

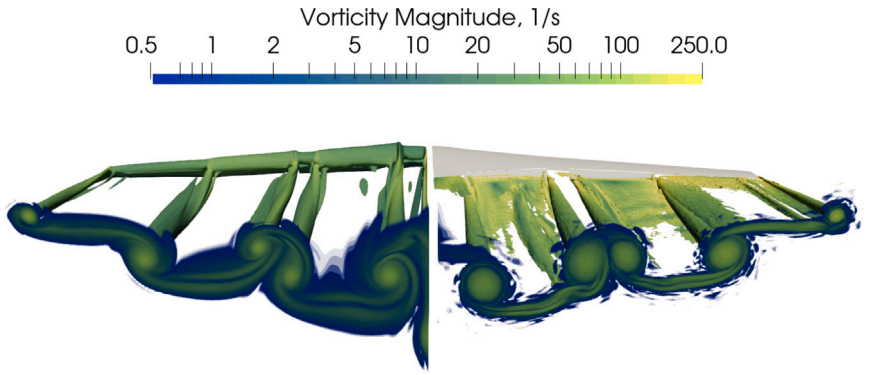

Fig. 9. Test Point 3 - Isosurfaces of Q-Criterion = 50 for ALM-ROM (Left), EETAR12 Explicit Simulation (Right).

from the ALM-ROM simulations was the presence of the shed vorticity sheet as visible in close proximity to the aircraft surface within the EETAR12 results on the right of the figures. The ALM-ROM approach inducing the formation of vortical structures through the direct application of body force terms resulted in the effects of the turbulent surface interactions and associated shed vorticity being significantly reduced. As the key aim of the ALM-ROM remains the study of the farfield wake dynamics where the shed vorticity has since been rolled-up within the vortex structures, the effect of the ALM-ROM neglecting surface effects was considered minimal.

Quantitative comparisons of the wake structures as generated by the ALM-ROM and the simulation of the EETAR12 were performed through sampling a two-dimensional slice of the domain normal to the freestream at a point ten meters downstream, measured from the wingtip of the EETAR12 and actuator-line as visible within the plots of Fig. 10.

The capabilities of the ALM-ROM for the reproduction of the EETAR12 wake vortices was assessed based upon the position and induced velocity profile of the wake vortices generated by the actuator-line. Fig. 11 presents two-dimensional contour plots of the Q-Criterion for the two-dimensional slices of the domain 10 m downstream for each of the three test point simulations of the EETAR12 and the actuator-line equivalent counterpart. Identified by closed contours are the wake vortices produced by the ALM-ROM and the explicit simulation of the EETAR12 geometry in red and black respectively. Spanwise positions

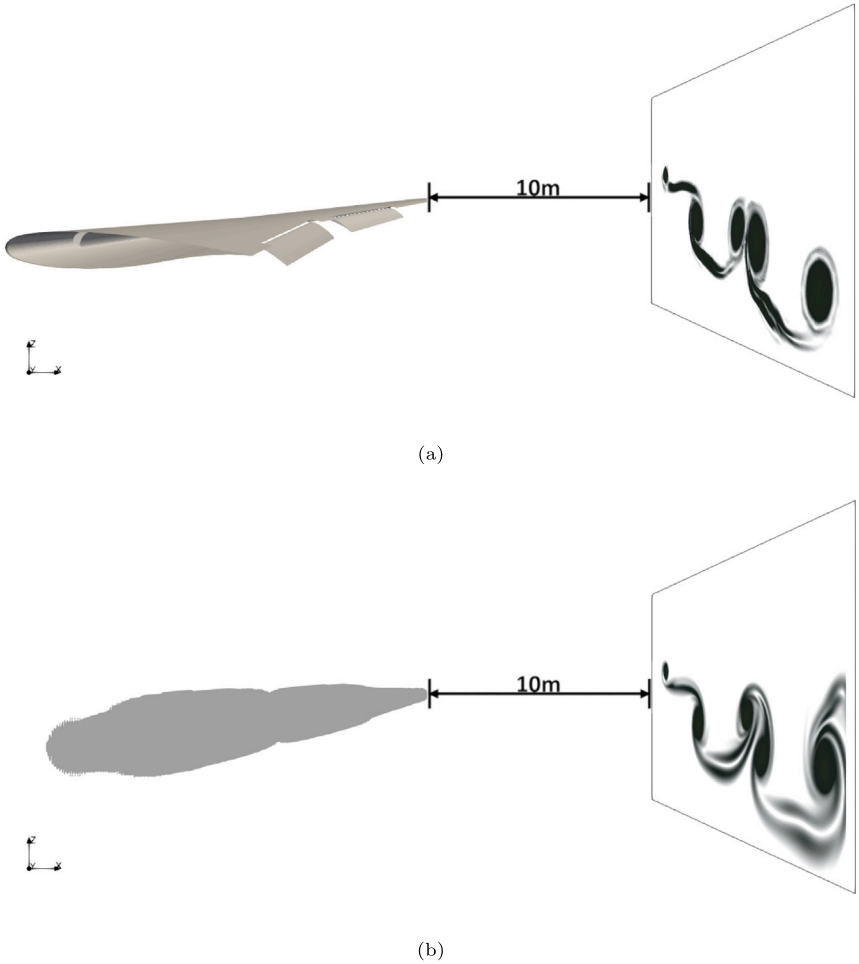

Fig. 10. Volumetric slice illustrations for EETAR12 geometric simulation (Above), ALM-ROM equivalent simulations (Below).

have been non-dimensionalised by the semi-span of the EETAR12 geometry. Comparing the results for each of the validation simulations, the ALM-ROM was able to replicate to a high degree of accuracy the location of the outermost vortices corresponding to the wingtip of the main wing and the outboard flap section both in terms of position and overall core radius. The greatest variations in both position and radii occurred for the vortices shed by the tip and root of the inboard and outboard flap sections respectively. Variations in vortex position were attributed to the use of single actuator-line for the combined slat, wing and flap geometries which following the integration process of Eq. (5) resulted in actuator-line nodes that lay upon the approximated aerodynamic centre of the main wing. Hence despite the effect of the high-lift devices being captured in the relevant aerodynamic force distributions, the information discerning the location of the flap sections relative to the main wing could not be maintained leading to the induction of vortices at relatively higher elevation as compared to the physical case. For the study of farfield behaviour where the inner wake vortices translate significantly leading to an eventual merging, the effect of a minor difference in initial position of the innermost structures was considered minimal. Variations in core size and hence vortex strength were attributed to the use of the convolution step in the initialisation of the body force terms within SU2. Such a step required for the numerical stability of the solver led to additional numerical dissipation and therefore reduced vorticity within the domain due to the distribution of the total applied force among surrounding grid points. Within each of the contour plots, small vortices were observed at the root of the actuator-line visible at the 0 m spanwise position for the ALM-ROM results. The formation of such additional vortices was a consequence of enforcing a wall symmetry condition. For the final application of the ALM-ROM method where the full EETAR12 wingspan would be simulated via the reflection of the spanwise distribution, the symmetry condition and associated additional vortices would be removed.

Wake velocity profiles were generated from the two-dimensional downstream slices via sampling of a polyline constructed from a series of straight line segments positioned in such a manner as to pass through each of the five wake vortex structures horizontally. Hence only the vertical velocity component of the velocity be considered. Plotted within Fig. 11 are the velocity profiles obtained from the EETAR12 simulations and their associated ALM-ROM equivalent result. Identifiable by the characteristically large fluctuations are the velocities across each of the five wake structures which when compared to the wake of the original EETAR12 results show good agreement both in terms of overall location and peak values. Similar to the analysis of the vortex position, numerical dissipation caused by the introduction of the convolution step in the application of ALM source terms was considered the source of velocity differences between the solutions by breaking the direct similarity to a true lifting-line [41]. Despite the ALM-ROM generating vortex structures with reduced velocities in the immediate nearfield, the ability to significantly refine the grid downstream led to a reduction in the overall amount of numerical dissipation present for farfield simulations employing the ALM-ROM.

Table 8, lists computational metrics for results obtained through the explicit simulation of the EETAR12 geometry and through using the coupled ALM-ROM approach for the case of flap configuration four. Both simulations were performed on the ARCHIE-WeSt computing cluster with 120 CPUs allowing valid comparisons to be drawn

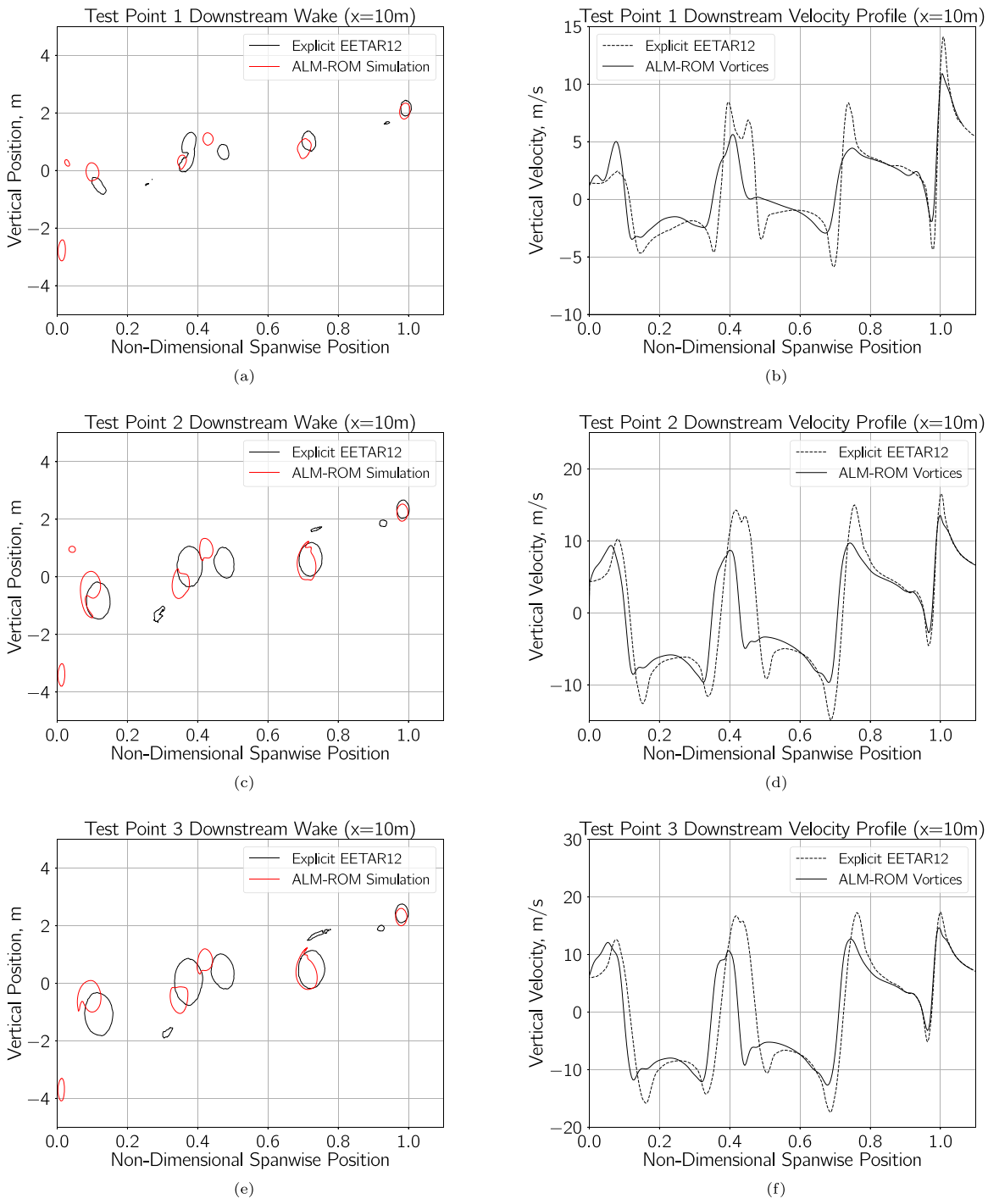

Fig. 11. Test point velocity profiles obtained from explicit EETAR12 simulation vs. ALM-ROM equivalent, Measured 10 m downstream.

regarding the computational cost of the respective approaches. On average, the simulation of the EETAR12 aircraft with the geometry present required less time per iteration to complete as compared with the ALM-ROM approach. The increase of time per iteration was a result of the additional steps required internally in assigning the source terms of the actuator-line which through improved coding practices may be further improved. In total the ALM-ROM required significantly less solver iterations to reach a converged state as compared to the original EETAR12 geometry simulations which when combined with the average iteration time demonstrate a reduction in total runtime between the two approaches. Considering the overall size of the grids used, the reduction in computational costs the ALM-ROM approach provides is further illustrated with the results obtained on a grid 25% larger than the EETAR12 geometry simulation. Regarding the study of vortex structures in particular, for the explicit simulation of the EETAR12 geometry, 70% of the computational grid was reserved solely for capturing surface and boundary layer effects. Compared to ALM-ROM simulations where the grid was substantially more refined in the wake vortex region, the benefits the ALM-ROM provide for the study of wake vortex structures becomes apparent by allowing greater levels of refinement surrounding the vortex core structures for a reduced computational cost.

For the purpose of studying wake structures generated by intermediate or varying high-lift configurations, the ALM coupled with the ROM

Table 8
Computational cost metrics for EETAR12 geometric simulation and ALM-ROM equivalent case.

	Time per iteration (s)	Number of iterations to converged state	Grid points	Number of CPUs
EETAR12 Explicit Simulations	8.99	3000	$\sim 17 \times 10^6$	120
ALM-ROM Equivalent Simulations	13.26	845	$\sim 22 \times 10^6$	120

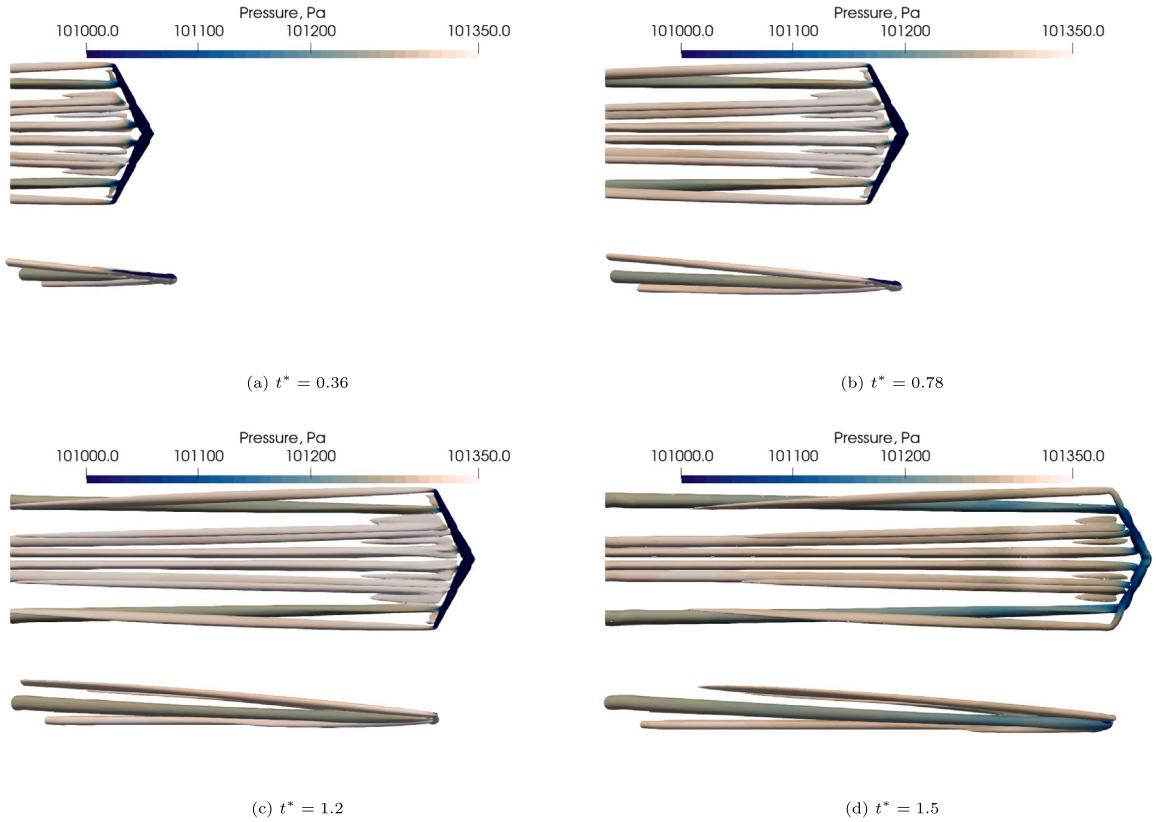

Fig. 12. Isosurfaces of Q-Criterion for unsteady ALM-ROM application case for non-dimensionalised time snapshots.

notably reduced the total time required from inception to results by several orders of magnitude. Once initialised, the ALM-ROM removed the need for the various solution based adaptation steps for the simulation of further aircraft configurations. Comparing the five simulations required for a single explicit simulation of the EETAR12 to the one required for ALM study, the savings are evident. For studies aimed at investigating vortex decay mechanisms and atmospheric boundary layer interactions the ALM-ROM method appears well suited for further applications.

4.3. Unsteady ALM-ROM approach path study

With the ALM-ROM approach fully validated, its application to the study of high-lift vortex dynamics in close proximity to the ground is demonstrated. By sweeping the actuator-line throughout the numerical domain on a per-timestep basis the wake system generated by the transit of the EETAR12 aircraft throughout a specific ground region of study could be observed. Fig. 12, shows the time evolution of the key wake vortex structures as represented by isosurfaces of the Q-Criterion. Within each of the subplots a top down view is presented (above) with a side-on view (below) indicating the trajectory of the actuator-line representation as it transits the simulation domain on a three degree glide slope. Subplots have been ordered according to their non-dimensionalised time, t^*, corresponding to the current physical time divided by the time taken for the actuator line to pass through the domain. Downstream of the actuator-line across all of the time instances shown the formation and propagation of the wake vortex phenomena appear visible within the wake region. For the present case with the complete span simulated, ten wake vortex structures were generated. The isosurfaces coloured by the pressure shows the relative strength of each of the structures as they evolve in time. Consistent with the previous results of the body-fixed actuator-line case, the tip vortex shed by the outer flap section possessed the lowest pressure distribution indicating a strong possibility of the final contra-rotating system to be composed of these two vortices across the span of the wake. In the side-on plots of Fig. 12 the descent of the innermost vortex pairs was observed, motivated by the mutual induction of their vertical velocity fields, these vortices descended significantly faster than their outermost counterparts. For the study of the ground impact such vortex systems may have, the likelihood of these vortex pairs impacting a structure and causing damage was increased. With the completion of the roll-up process, the system presented within Fig. 12 could be propagated further for the study of vortex farfield behaviour within the same computational environment. Simulation of the complete span negating the need for a symmetry boundary eliminated the occurrence of the minor coherent structures that were visible in the stationary validation cases. Following the results of both the body-fixed actuator-line validation cases and the ground-fixed unsteady translating actuator-line case the robustness of the ALM-ROM method was demonstrated. There continues to exist a clear need to understand wake vortex phenomena

as shed by high-lift geometries in the near ground environment for which the current ALM-ROM approach appears promising.

5. Conclusion

The setup and implementation of the ALM-ROM method within the SU2 framework has now been presented and validation tests performed comparing the wake vortices generated by the new approach to conventional simulations of the EETAR12 high-lift aircraft geometry. The capability of the ALM-ROM to reproduce wake vortex systems has been evaluated based upon the velocity profile and core position as measured downstream, the results of which show a high level of agreement particularly for the outermost two vortices of the five vortex semi-span system. With the creation of the ROM, the ability to simulate the wake generated by the EETAR12 aircraft at untested flap deflection angles became simplified reducing the need for further high-fidelity simulations of the EETAR12 geometry and associated mesh adaptation steps cutting the number of simulations from five to one. Through the completion of the current work the ALM-ROM method may be adopted for the higher-fidelity simulation of similarly configured high-lift aircraft on approach or take-off trajectories as demonstrated in the application of the ALM-ROM to the study of an aircraft on final approach. The results obtained via the ALM-ROM approach being given in full confidence that results provided remain highly-physical with respect to the key flow-physics on display. Through the ALM-ROM approach the range of operating scenarios that may be simulated has been extended significantly. The aforementioned method thus improving wake vortex simulation capabilities for aircraft in ground proximity lays the foundation for future ALM simulations focused on examining specific wake dynamics that reinforce cohesive arguments regarding the alteration of mandatory aircraft separation distances and the benefits they may provide.

CRediT authorship contribution statement

S. Bennie: Writing – review & editing, Writing – original draft, Visualization, Methodology, Investigation, Conceptualization. **P. Nagy:** Writing – original draft, Software. **M. Fossati:** Writing – review & editing, Supervision, Project administration, Conceptualization.

Funding sources

Funding for this work was kindly provided in partnership between the University of Strathclyde and AGS Airports.

Declaration of competing interest

The authors declare the following financial interests/personal relationships which may be considered as potential competing interests: Associate Editor of the Computers and Fluids journal, M. Fossati If there are other authors, they declare that they have no known competing financial interests or personal relationships that could have appeared to influence the work reported in this paper.

Acknowledgements

The authors would like to acknowledge the contributions of the SU2 community to the development of a robust open-source CFD software in addition to the ARCHIE-WeSt High Performance Computer (www.archie-west.ac.uk) based at the University of Strathclyde. The authors would also like to thank AGS airports for their contributions to the project in providing funding and support.

Data availability

The data that has been used is confidential.

References

[1] Gerz T, Holzäpfel F, Darracq D. Commercial aircraft wake vortices. Prog Aerosp Sci 2002;38(3):181–208. http://dx.doi.org/10.1016/S0376-0421(02)00004-0.
[2] Hallock JN, Holzäpfel F. A review of recent wake vortex research for increasing airport capacity. Prog Aerosp Sci 2018;98:27–36. http://dx.doi.org/10.1016/j.paerosci.2018.03.003.
[3] Hahn K-U, Schwarz C. Wake vortex avoidance versus landing capacity. In: AIAA guidance, navigation, and control conference and exhibit. AIAA; 2006, http://dx.doi.org/10.2514/6.2006-6322.
[4] Holzäpfel F, Gerz T, Frech M, Tafferner A, Köpp F, Smalikho I, Rahm S, Hahn K-U, Schwarz C. The wake vortex prediction and monitoring system WSVBS part I: Design. Air Traffic Control Q 2009;17(4):301–22. http://dx.doi.org/10.2514/atcq.17.4.301.
[5] Hallock JN, Tung CY, Sampath S. Capacity and wake vortices. In: 23rd inernational congress of aeronautical sciences. 2002, URL https://api.semanticscholar.org/CorpusID:30329776.
[6] US Department of Transportation. Aircraft wake turbulence - advisory circular. Tech. rep., Federal Aviation Administration; 2014, URL https://www.faa.gov/documentLibrary/media/Advisory_Circular/AC_90-23G.pdf.
[7] Rutishauser DK, O'Connor CJ. The NASA aircraft vortex spacing system (AVOSS): Concept demonstration results and future direction. Tech. rep., National Aeronautics and Space Administration; 2004.
[8] Lau A, Lorenz S. Individual wake vortex separations: Capacity and delay impact on single and dual dependent runway systems. In: 12th AIAA aviation technology, integration, and operations (ATIO) conference and 14th AIAA/ISSMO multidisciplinary analysis and optimization conference. AIAA; 2012, http://dx.doi.org/10.2514/6.2012-5641.
[9] Rooseleer F, Treve V. ""RECAT-EU" European wake turbulence categorisation and separation minima on approach and departure". Tech. rep., EUROCONTROL; 2018.
[10] Blackmore P. The effects of aircraft trailing vortices on house roofs. J Wind Eng Ind Aerodyn 1994;52:155–70. http://dx.doi.org/10.1016/0167-6105(94)90045-0.
[11] Uhl A, Braun S, Stumpf E. Experimental and numerical investigation of the interaction of wake vortices with a gable roof. In: New results in numerical and experimental fluid mechanics XII. Cham: Springer International Publishing; 2020, p. 447–56.
[12] Czech M, Miller G, Crouch J, Strelets M. Predicting the near-field evolution of airplane trailing vortices. C R Phys 2005;6(4):451–66. http://dx.doi.org/10.1016/j.crhy.2005.05.005, Aircraft trailing vortices.
[13] Ahmad NN. Numerical simulation of the aircraft wake vortex flowfield. In: 5th AIAA atmospheric and space environments conference. AIAA; 2013, http://dx.doi.org/10.2514/6.2013-2552.
[14] Breitsamter C. Wake vortex characteristics of transport aircraft. Prog Aerosp Sci 2011;47(2):89–134. http://dx.doi.org/10.1016/j.paerosci.2010.09.002.
[15] Kuenn AD, Kliment LK. A brief survey of vortex models. In: AIAA scitech 2021 forum. AIAA; 2021, http://dx.doi.org/10.2514/6.2021-1328.
[16] Ahmad NN, Proctor F. Review of idealized aircraft wake vortex models. In: 52nd aerospace sciences meeting. AIAA; 2014, http://dx.doi.org/10.2514/6.2014-0927.
[17] Misaka T, Holzäpfel F, Gerz T. Large-eddy simulation of aircraft wake evolution from roll-up until vortex decay. AIAA J 2015;53(9):2646–70. http://dx.doi.org/10.2514/1.J053671.
[18] Zhang J-D, Zuo Q-H, Lin M-D, Huang W-X, Pan W-J, Cui G-X. Evolution of vortices in the wake of an ARJ21 airplane: Application of the lift-drag model. Theor Appl Mech Lett 2020;10(6):419–28. http://dx.doi.org/10.1016/j.taml.2020.01.054.
[19] Stephan A, Holzäpfel F, Misaka T. Hybrid simulation of wake-vortex evolution during landing on flat terrain and with plate line. Int J Heat Fluid Flow 2014;49:18–27. http://dx.doi.org/10.1016/j.ijheatfluidflow.2014.05.004, 8th Symposium on Turbulence & Shear Flow Phenomena (TSFP8).
[20] Lin M, Cui G, Zhang Z. A new vortex sheet model for simulating aircraft wake vortex evolution. Chin J Aeronaut 2017;30(4):1315–26. http://dx.doi.org/10.1016/j.cja.2017.04.015.
[21] Zhou J, Chen Y, Li D, Zhang Z, Pan W. Numerical simulation of aircraft wake vortex evolution and wake encounters based on adaptive mesh method. Eng Appl Comput Fluid Mech 2020;14(1):1445–57. http://dx.doi.org/10.1080/19942060.2020.1835736.
[22] Sørensen JN, Shen WZ. Numerical modeling of wind turbine wakes. J Fluids Eng 2002;124(2):393–9. http://dx.doi.org/10.1115/1.1471361.
[23] Crow SC. Stability theory for a pair of trailing vortices. AIAA J 1970;8(12):2172–9. http://dx.doi.org/10.2514/3.6083.
[24] Merabet R, Laurendeau E. Hovering helicopter rotors modeling using the actuator line method. J Aircr 2022;59(3):774–87. http://dx.doi.org/10.2514/1.C036314.
[25] Kim D, Lee Y, Oh S, Park Y, Choi J, Park D. Aerodynamic analysis and static stability analysis of manned/unmanned distributed propulsion aircrafts using actuator methods. J Wind Eng Ind Aerodyn 2021;214:104648. http://dx.doi.org/10.1016/j.jweia.2021.104648.

[26] Kleine VG, Hanifi A, Henningson DS. Simulating airplane aerodynamics with body forces: Actuator line method for nonplanar wings. AIAA J 2023;61(5):2048–59. http://dx.doi.org/10.2514/1.J062398.
[27] Economon TD, Palacios F, Copeland SR, Lukaczyk TW, Alonso JJ. SU2: An open-source suite for multiphysics simulation and design. AIAA J 2016;54(3):828–46. http://dx.doi.org/10.2514/1.J053813.
[28] Morgan Jr HL, Paulson Jr JW. Low-speed aerodynamic performance of a high-aspect-ratio supercritical-wing transport model equipped with full-span slat and part-span double-slotted flaps. Tech. rep., NASA; 1979.
[29] Olson ED. Three-dimensional modeling of aircraft high-lift components with vehicle sketch pad. In: 54th AIAA aerospace sciences meeting. AIAA; 2016, http://dx.doi.org/10.2514/6.2016-1274.
[30] Geuzaine C, Remacle J-F. Gmsh: A 3-D finite element mesh generator with built-in pre- and post-processing facilities. Internat J Numer Methods Engrg 2009;79(11):1309–31. http://dx.doi.org/10.1002/nme.2579.
[31] Marcum DL, Alauzet F, Loseille A. On a robust boundary layer mesh generation process. In: 55th AIAA aerospace sciences meeting. AIAA; 2017, http://dx.doi.org/10.2514/6.2017-0585.
[32] Delisi D, Greene G, Robins R, Vicroy D, Wang F. Aircraft wake vortex core size measurements. In: 21st AIAA applied aerodynamics conference. AIAA; 2003, http://dx.doi.org/10.2514/6.2003-3811.
[33] Spalart P, Allmaras S. A one-equation turbulence model for aerodynamic flows. In: 30th aerospace sciences meeting and exhibit. AIAA; 1994, http://dx.doi.org/10.2514/6.1992-439.
[34] Sirovich L. Turbulence and the dynamics of coherent structures. I - Coherent structures. II - symmetries and transformations. III - dynamics and scaling. Quart Appl Math 1987;45. http://dx.doi.org/10.1090/qam/910463.
[35] Bui-Thanh T, Damodaran M, Willcox K. Proper orthogonal decomposition extensions for parametric applications in compressible aerodynamics. In: 21st AIAA applied aerodynamics conference. AIAA; 2003, http://dx.doi.org/10.2514/6.2003-4213.
[36] Holmes P, Lumley JL, Berkooz G. Turbulence, coherent structures, dynamical systems and symmetry. Cambridge monographs on mechanics, Cambridge University Press; 1996, http://dx.doi.org/10.1017/CBO9780511622700.
[37] Karcher N, Franz T. Adaptive sampling strategies for reduced-order modeling. CEAS Aeronaut J 2022;13(2):487–502. http://dx.doi.org/10.1007/s13272-022-00574-6.
[38] Mikkelsen R, et al. Actuator disc methods applied to wind turbines [Ph.D. thesis, PhD thesis], Technical University of Denmark; 2003.
[39] Weihing P, Schulz C, Lutz T, Krämer E. Comparison of the actuator line model with fully resolved simulations in complex environmental conditions. J Phys: Conf Ser 2017;854(1):012049. http://dx.doi.org/10.1088/1742-6596/854/1/012049.
[40] Shives M, Crawford C. Mesh and load distribution requirements for actuator line CFD simulations. Wind Energy 2013;16(8):1183–96. http://dx.doi.org/10.1002/we.1546.
[41] Forsting ARM, Pirrung GR, Ramos-García N. The wake of an actuator line with a vortex-based tip/smearing correction in uniform and turbulent inflow. J Phys: Conf Ser 2019;1256(1):012020. http://dx.doi.org/10.1088/1742-6596/1256/1/012020.